ADVANCED ELECTRONIC MATERIALS
Open Access
www.advelectronicmat.de

Defect Density of States of Tin Oxide and Copper Oxide *p*-type Thin-film Transistors

Måns J. Mattsson, Kham M. Niang, Jared Parker, David J. Meeth, John F. Wager, Andrew J. Flewitt, and Matt W. Graham**

The complete subgap defect density of states (DoS) is measured using the ultrabroadband (0.15 to 3.5 eV) photoconduction response from p-type thin-film transistors (TFTs) of tin oxide, SnO, and copper oxide, Cu_2O. The resulting TFT photoconduction spectra clearly resolve bandgaps that show the presence of interfacial and oxidized minority phases. In tin oxide, the SnO majority phase has a small 0.68 eV bandgap enabling ambipolar or p-mode TFT operation. By contrast, in copper oxide TFTs, an oxidized minority phase with a 1.4 eV bandgap corresponding to CuO greatly reduces the channel hole mobility at the charge accumulation region. Three distinct subgap DoS peaks are resolved for the copper oxide TFT and are best ascribed to copper vacancies, oxygen-on-copper antisites, and oxygen interstitials. For tin oxide TFTs, five subgap DoS peaks are observed and are similarly linked to tin vacancies, oxygen vacancies, and oxygen interstitials. To achieve desirable unipolar p-mode TFTs, the conduction band-edge defect density of oxygen interstitials must be sufficiently large to suppress n-mode conduction. In both channel materials, the metal vacancy peak densities near the valence band edge determine the hole concentrations, which then predict the TFT Fermi level energy, observed on-off ratios, and threshold voltages.

1. Introduction

Reliable p-type metal oxide materials remain elusive despite the widespread adoption of n-type metal oxide thin-film transistors (TFTs) for applications such as display panels. Several fundamental and practical barriers prevent p-type TFTs from achieving the same high mobility and low leakage currents that are now celebrated in n-type materials such as amorphous indium gallium zinc oxide (a-IGZO).[1–4] Most metal oxide semiconductors are inherently oxygen-deficient and thus n-type. Even at large gate voltages, p-type behavior is difficult to achieve due to the deleterious effects of very large Urbach energies (E_U = 90-120 meV), with correspondingly large hole trap densities. To show how subgap defect states enable successful p-mode operation in metal oxide TFTs, this work measures the subgap integrated trap density using the ultrabroadband photoconductive density of states (UP-DoS) method.[5,6]

Over the past decade, many p-type metal oxide semiconductors have been suggested, including NiO, TeO_2, CuO, and different types of spinel oxides.[7–10] Two of the most promising active channel material candidates for p-mode oxide TFTs are tin and copper oxide with a typical hole mobility of 1–2 cm^2 V^{-1} s^{-1} and reported on-to-off ratios of $\approx 10^3 - 10^5$.[11–13] While considerable improvement of p-type TFTs is anticipated, p-type TFT device properties are not yet commensurate with typical n-mode metal oxide TFTs that now have mobilities >10 cm^2 V^{-1} s^{-1} and on-to-off ratios approaching 10^{12}.[14,15] The discovery of more viable metal oxide p-type TFTs remains critical for beyond-silicon complementary metal oxide semiconductor (CMOS) needed for conventional von Neumann computing architectures. Likewise, emerging neuromorphic computer architectures and memory technologies seek to exploit the metal and oxygen vacancy defects in p-type TFTs.[16,17]

One necessary condition for robust p-mode TFT operation is sharp valence band tail states with small Urbach energies. In metal oxides, such small tail energies at valence band maximum are rare owing to an overwhelmingly large anionic disorder created by oxygen 2p-orbital interactions. In addition to the large

M. J. Mattsson, J. Parker, M. W. Graham
Department of Physics
Oregon State University
Corvallis, OR 97331, USA
E-mail: graham@physics.oregonstate.edu
K. M. Niang, D. J. Meeth, A. J. Flewitt
Electrical Engineering Division
University of Cambridge
CB3 0FA Cambridge, UK
E-mail: ajf23@cam.ac.uk
J. F. Wager
School of EECS
Oregon State University
Corvallis, OR 97331, USA

The ORCID identification number(s) for the author(s) of this article can be found under https://doi.org/10.1002/aelm.202400929

© 2025 The Author(s). Advanced Electronic Materials published by Wiley-VCH GmbH. This is an open access article under the terms of the Creative Commons Attribution License, which permits use, distribution and reproduction in any medium, provided the original work is properly cited.

DOI: 10.1002/aelm.202400929

effective mass of the asymmetric 2p-orbitals limiting mobility, the resulting broad valence band maximum Urbach tails lead to a high concentration of localized tail states, which act as hole traps. [18,19] Unusual for metal oxides, orbital theory in tin and copper oxide predicts that the valence band maximum band-edge states may have strong Sn-5s and Cu-3d orbital character that may compete with oxygen-2p disorder to form the highest occupied molecular orbital.[20,21] The diffuse and symmetric orbitals of the Sn-5s and Cu-3d contributions further help explain the higher mobilities and smaller hole effective mass reported in the literature.[12,20,22,23]

Electronic structure and density functional theory (DFT) simulations widely attribute metal vacancies as the origin of preferential effective p-type doping of tin oxide and copper oxide TFTs.[24–28] There is considerable disagreement between different DFT studies on the exact structure and metal vacancy placement within the subgap relative to the many other significant defect peaks predicted.[24–28] Previous experimental studies use field-effect conductance or CV-methods, and provide valuable insight on the near band regions only.[29–31] Instead, the UP-DoS method uses scanning laser microscopy over a tunable $h\nu$ = 0.15 to 3.5 eV range to obtain a photoconduction (PC) spectrum proportional to the total integrated trap density, and thereby obtain the subgap defect density of states (DoS) for tin and copper oxide TFTs.

2. Results and Discussion

Figure 1a shows the cross-section of tin and copper oxide TFTs with their associated photoconduction (PC) microscopy map in the lower panel. The measured transfer curves (W/L = 10, V_{SD} = 1 V) shown in Figure 1b of tin oxide and copper oxide TFTs both show characteristic p-mode behavior with a negative gate voltage turn-on and ≈10^5 and ≈10^4 on-to-off ratios, respectively. Clockwise hysteresis due to hole trapping and re-emission is pronounced for both types of TFTs. Figure 1c presents indirect Tauc-like plots of normalized TFT photoconductance [$(I_{norm}h\nu)^{1/2}$ versus hν] that are shown as solid lines. For tin oxide, the estimated indirect bandgap is equal to 0.68 eV, corresponding to SnO, in good agreement with reported values for SnO of 0.70–0.75 eV.[32,33] For copper oxide, the estimated indirect bandgap is found to be 1.4 eV, corresponding to CuO. Also shown in Figure 1c are direct gap Tauc plots [$(\alpha h\nu)^2$ versus hν] from thin-film absorption data (dashed lines). A direct bandgap of 2.9 eV is found for tin oxide, corresponding to SnO, while a direct bandgap of 2.4 eV is estimated for copper oxide, consistent with Cu_2O. **Table 1** summarizes the bandgaps retrieved from photoconduction and absorption measurements, along with their comparisons of DFT calculated values reported in the literature.

Figure 1d shows a comparison of absorption (black) and photoconductance (blue for tin oxide; green for copper oxide). Abrupt thresholds in which absorption increases while photoconductance decreases of 3.5 eV for tin oxide and 2.4 eV for copper oxide provide strong evidence for the presence of SnO_2 and Cu_2O, respectively. The *inset* of Figure 1d further shows the total raw photoconductance spectrum drops off by a factor of 10^5 for tin oxide and 10^7 for copper oxide, as subgap defect states are photoexcited below the respective indirect bandgaps of SnO and CuO.

Taken together, Figure 1c,d provide strong evidence that both the tin oxide and copper oxide thin-films are mixed-phase systems corresponding to SnO & SnO_2 and CuO & Cu_2O, respectively. Since XRD characterization shows no evidence of SnO_2 and CuO in these thin-films, we conclude that CuO and SnO_2 are minority phases compared to Cu_2O and SnO.[39,40] For copper oxide, the measured Hall mobility ($\mu_{Hall} = 20$ cm^{2}Vs^{-1}) is consistent with Cu_2O while the measured field-effect mobility (μ_{FE} = 0.1 cm^{2}Vs^{-1}) is most likely due to CuO. Similar mobility properties have been widely reported in the literature. [41–43] As TFT photoconductance is primarily sensitive to the charge accumulation layer, this supports that the Cu_2O-SiO_2 (semiconductor-dielectric) interface is heavily oxidized to CuO. [44] [45]

2.1. Ambipolar SnO Subgap DoS

Figure 2a plots the ambipolar SnO TFT transfer curve, and delineates the p-mode and n-mode conduction region where the UP-DoS spectra are taken. The SnO bandgap is identified in Figure 2b by applying Tauc scaling to the raw $I_{norm}(h\nu)$ signal. The extracted bandgap of E_g = 0.68 eV is in good agreement with previously reported 0.70–0.75 eV SnO bandgaps.[32,33] Figure 2c (*upper panel*) plots the integrated trap density, $N_{tot}(h\nu)$, for p-mode (blue line, V_G = −20 V) and n-mode (orange line, V_G = 27 V) operation. $N_{tot}(h\nu)$ is directly proportional to measured TFT photoconductance, and the subgap region consists of a sequence of step-wise features, where each step corresponds to a Gaussian peak in the subgap DoS shown by the dashed lines connected to the lower panel. Each subgap step in $N_{tot}(h\nu)$ is analytically fit to an error function (erf, solid line). The above-bandgap response is fit to an indirect absorption lineshape function (dashed lines) accounting for valence band to conduction band transitions. Note that plotting both the p-mode and n-mode signal on the same energy axis requires that the n-mode energy axis be shifted by $E_V + E_{h\nu} = -(E_C - E_{h\nu} - E_g)$, where $E_V + E_{h\nu}$ is the energy-axis of p-mode (VBM = 0), and $E_C - E_{h\nu}$ is the energy axis of n-mode (CBM = 0).

Figure 2c (lower panel) plots the SnO subgap DoS across the full bandgap. This is quite extraordinary since all prior UP-DoS measurements were conducted using unipolar semiconductors, where measuring the critical subgap states within a few k_bT to the active band edge was not possible. Note that the DoS shown in the lower panel of Figure 2c is obtained by differentiating upper panel data, i.e., DoS = $\frac{dN_{tot}}{d(h\nu)}$. Since each step in the N_{tot} data is fit to an erf, each N_{tot} step yields a corresponding Gaussian in the DoS plot. The use of error function fitting prior to differentiating significantly improves the DoS signal-to-noise ratio compared to simple point-by-point numerical differentiation of the raw N_{tot} data. Table 2 summarizes the parameters of each subgap DoS peak, numbered 1–5.

The identities of SnO subgap peaks 1–5 in Figure 2c are ascribed by comparison to the DFT calculations of Varley et al.[38] Subgap peaks in SnO are assigned as: 1. tin vacancy + hydrogen defect (V_{Sn} + H, acceptor), 2. tin vacancy (V_{Sn}, acceptor), 3. oxygen vacancy (V_O, donor), 4. hydrogen on an oxygen site (H_O, donor) and 5. oxygen interstitial (O_i, acceptor). While the tin and oxygen vacancy peaks are expected, peaks 1 and 5 require more discussion.

© 2025 The Author(s). Advanced Electronic Materials published by Wiley-VCH GmbH

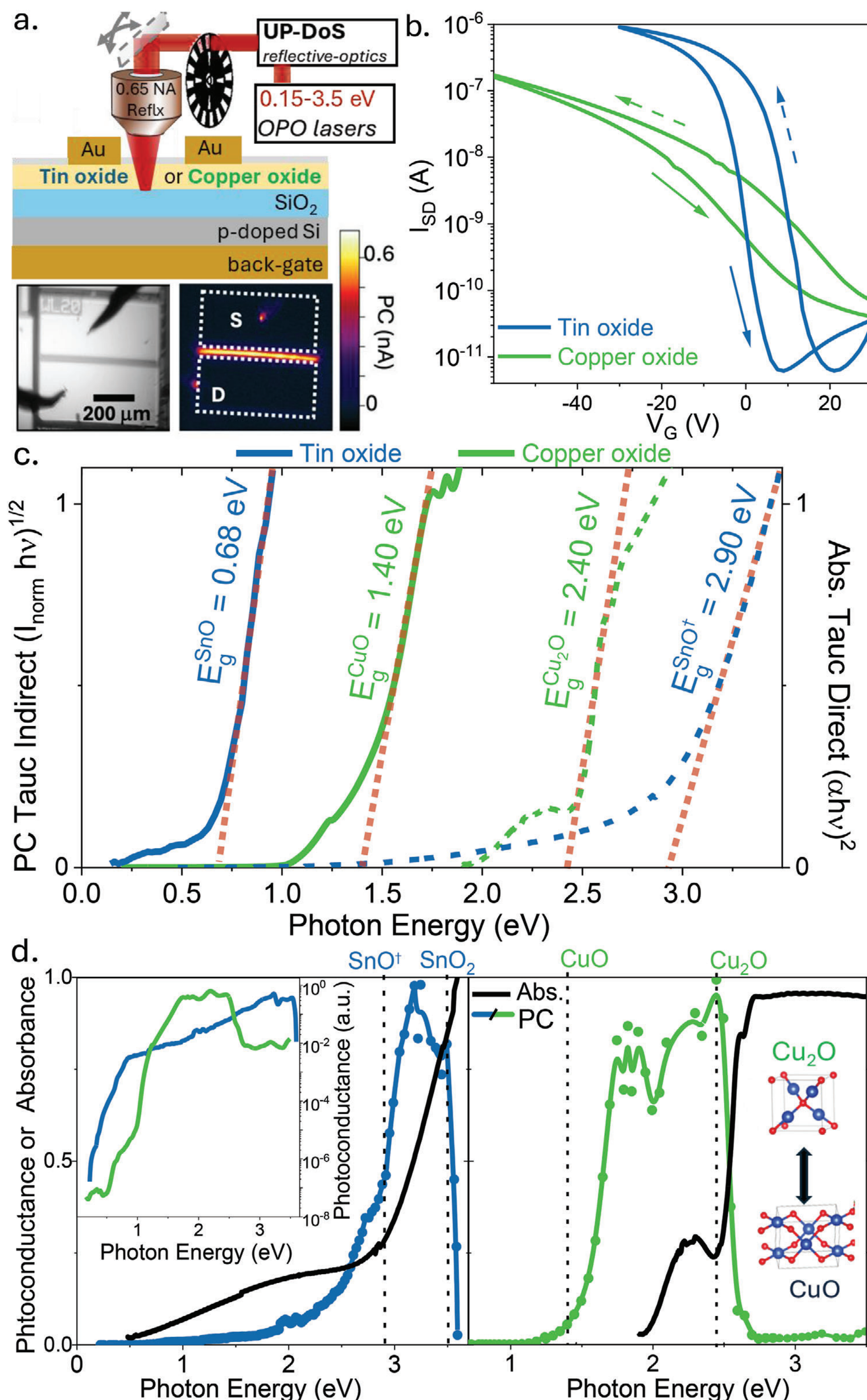

Figure 1. a) (top) TFT layer cross-section sketched with the basic UP-DoS measurement setup shown. (bottom) Copper oxide TFT reflection and photoconductance (PC) spatial maps for $h\nu = 1.1$ eV. b) TFT transfer curves of tin (blue) and copper (green) oxide. c) Solid lines show normalized TFT PC plotted with Tauc-like scaling $[(I_{norm}h\nu)^{1/2}]$ yielding an indirect bandgap of 0.68 eV corresponding to SnO and 1.4 eV corresponding to CuO. Dashed lines plot the Tauc absorption spectra scaled as $[(\alpha h\nu)^2]$ tio show a direct bandgap of 2.9 eV corresponding to SnO, and 2.4 eV corresponding to Cu_2O. d) At the labeled SnO_2 and Cu_2O direct bandgaps, the absorption spectrum (black) rises, while the PC-spectrum (blue/green) falls. (inset) The same TFT PC-spectra plotted on a logarithmic scale.

© 2025 The Author(s). Advanced Electronic Materials published by Wiley-VCH GmbH

Table 1. Measured (see Figure 1c; Figure S1, Supporting Information) and literature bandgaps for tin and copper oxide TFTs. † Direct-bandgap, *Indirect-bandgap transition too weak to optically resolve.

	Absorbance E_g^{abs} [eV]	Photoconduction $E_g^{UP\text{-}DoS}$ [eV]	Literature E_g [eV]
SnO	*indirect**	0.68	0.70–0.75 [32,33]
SnO†	2.9	2.9	2.8–3.0 [34]
SnO_2†	3.6	3.5	3.5–3.7 [33,35]
CuO	*indirect**	1.4	1.5 [36]
Cu_2O†	2.4	2.4	2.0–2.6 [36,37]

Figure 2c shows peak 1 is observedin both n- and p-mode UP-DoS measurements at a photon energy 0.02 eV above the bandgap. Thus, in principle, peak 1 could be positioned 0.02 eV below E_V or above E_C. Since peak 1 is observed to have the largest density of all peaks, it is assigned to the defect with the lowest formation energy, V_{Sn}+H located at the VB edge, as identified by Varley et al.

Varley et al. simulate a hydrogen interstitial donor defect with transition energy of ≈0.6 eV from the valence band maximum,[38] which could potentially correspond to peak 5 measuredat 0.66 eV in **Figure 3**b. However, from charge balance considerations, peak 5 needs to be a neutral acceptor rather than a positively charged ionized donor. Therefore, we propose an oxygen interstitial O_i acceptor as an alternative identification for this peak. While DFT studies calculate a low formation energy for this defect, they also predict a transition energy above the bandgap rather than near the conduction band minimum. [24,25,38,46] As a consequence of the SnO lattice coplanar layered structure, oxygen interstitials are suspected to be abundant at the oxidized interface between SnO and SnO_2. [46,47]

2.2. P-Type SnO Subgap DoS

Figure 3 shows the evolution of the SnO subgap DoS from p-mode to ambipolar TFT behavior. Figure 3a shows three SnO TFT transfer curves (W/L = 10, V_{SD} = 1 V) classified as p-type (black), weak-ambipolar (250 °C annealed, purple), and strong-ambipolar (350 °C annealed, blue). The corresponding integrated trap densities, N_{tot}, are shown in Figure 3b (upper panel). Using orange circles, just one example of a n-mode N_{tot} spectrum is plotted in Figure 3b (upper panel) corresponding to the most clearly ambipolar TFT in 3a (blue). Indicated by the vertical dashed lines, Figure 3b (upper panel) shows five subgap steps labeled 1–5 that correspond to Gaussian DoS peaks shown in Figure 3b (lower panel). The peaks observed and their identifications match those previously discussed in Figure 2.

The lower panel of Figure 3b further shows that as SnO changes with annealing conditions from p-type to ambipolar behavior, a corresponding decrease in subgap defect density is observed. The significant enhancement in n-mode behavior with annealing that is observed in Figure 3a is attributed primarily to a decrease of the defect peak located just below the conduction band minimum, identified as O_i. Note that for

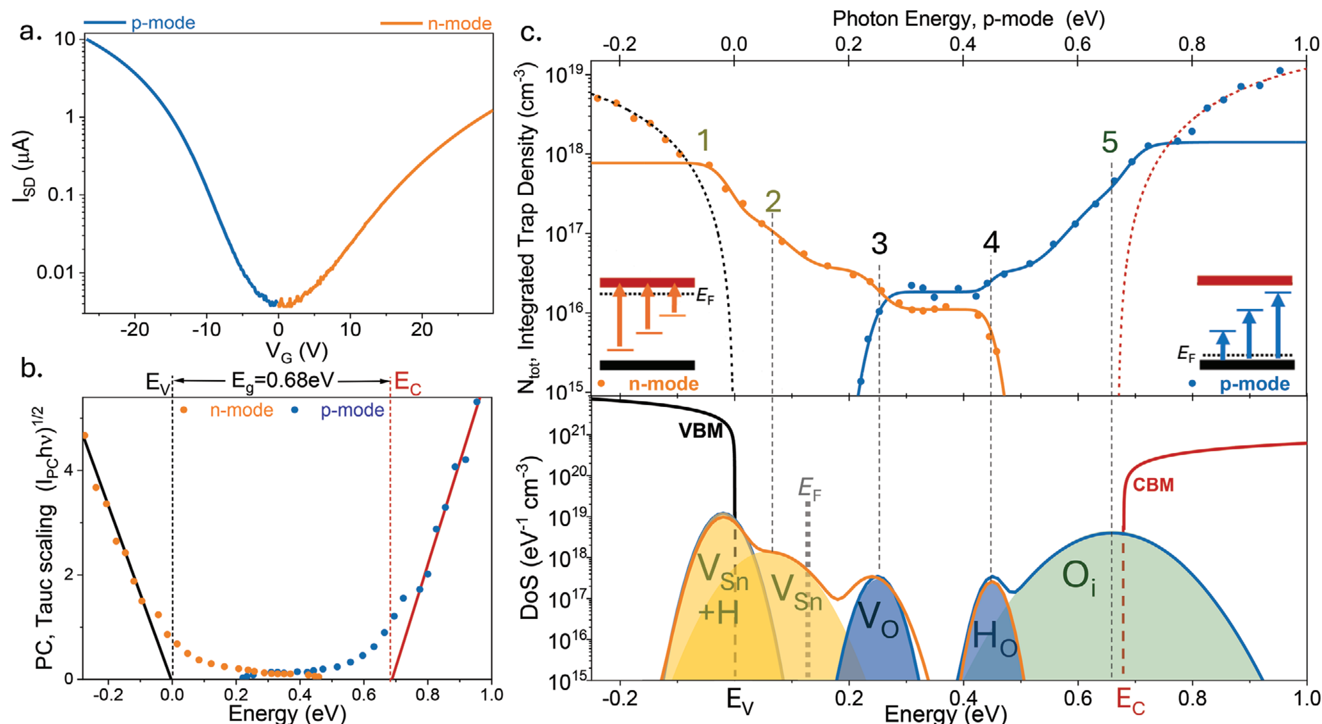

Figure 2. Ambipolar tin oxide subgap DoS a) TFT transfer curve of ambipolar SnO (W/L = 100) at V_{SD} = 1 V for p-mode (blue) and n-mode (orange) operation. b) Tauc scaling of the photoconduction taken in n-mode (orange) and p-mode (blue) showing a SnO bandgap of 0.68 eV. c) Upper panel plots the SnO integrated trap density, N_{tot}, measured at p-mode and n-mode TFT gate voltages. Lower panel plots the corresponding DoS of SnO that reveals five numbered subgap peaks with suggested defect assignments according to **Table 2**.

© 2025 The Author(s). Advanced Electronic Materials published by Wiley-VCH GmbH

Table 2. Estimated subgap DoS parameters from UP-DoS measurements of the ambipolar SnO TFT plotted in Figure 2c are compared to DFT calculated values by Varley et al. [38] The UP-DoS results and DFT show good agreement both in terms of defect prevalence and energetic position.

DoS Peak	Assigned Defect	Peak Energy [eV]	FWHM [meV]	Peak DoS × 10^{17} [$cm^{-3}eV^{-1}$]	DFT Formation Energy[38] [eV]	DFT Peak Energy[38] [eV]
1	V_{Sn}+H	−0.02	25	120.6	0.6	0.07
2	V_{Sn}	0.06	46	13.3	1.5	0.13
3	V_O	0.25	21	3.2	1.4	0.24
4	H_O	0.45	16	2.7	1.2	0.60
5	O_i	0.66	63	39.2	1.1	>0.7

n-mode operation, O_i behaves as an electron trap.[48] To achieve unipolar p-type SnO TFT operation with low off current, similar to the black curve of 3a, $[O_i]$ should be sufficiently large to suppress the undesired n-mode behavior. Accordingly, high on-to-off ratios of 10^5 for unipolar p-type TFTs are observed only when the conduction band-edge oxygen interstitial defect density is large enough to suppress off-current n-mode conduction.

To further connect device performance characteristics with experimental peak defect DoS, the Fermi level energy and observed threshold voltage are simulated from first-principles in Experimental Section 4 using charge balance and the discrete trap model. Figure 3c presents a simulation of the Fermi level energy together with the p- and n-mode threshold voltages as a function of $[V_{Sn}$+H]. The dashed vertical lines indicate the measured defect density of each TFT, whereas the horizontal dashed arrows are visual aids to guide each simulated parameter to the correct y-axis. When $[V_{Sn}+H] > \approx 10^{17}$ cm^{-3} (as observed for all three TFTs), the simulation shows that $[V_{Sn}$+H] controls the Fermi energy, and consequently the threshold voltage, whereas to a good approximation $p \approx [V_{Sn}+H]$. Furthermore, Figure 3c shows that when $[V_{Sn} + H] < \approx 10^{18}$ cm^{-3}, both n- and p-mode threshold voltages are easily accessible, enabling ambipolar TFT behavior. Additionally, by using the relationship shown in Figure 3c, it is possible to accurately estimate the defect density, $[V_{Sn}$+H], and the Fermi level energy, E_F, based solely of the threshold voltage of a device (see Section S2, Supporting Information for specific details).

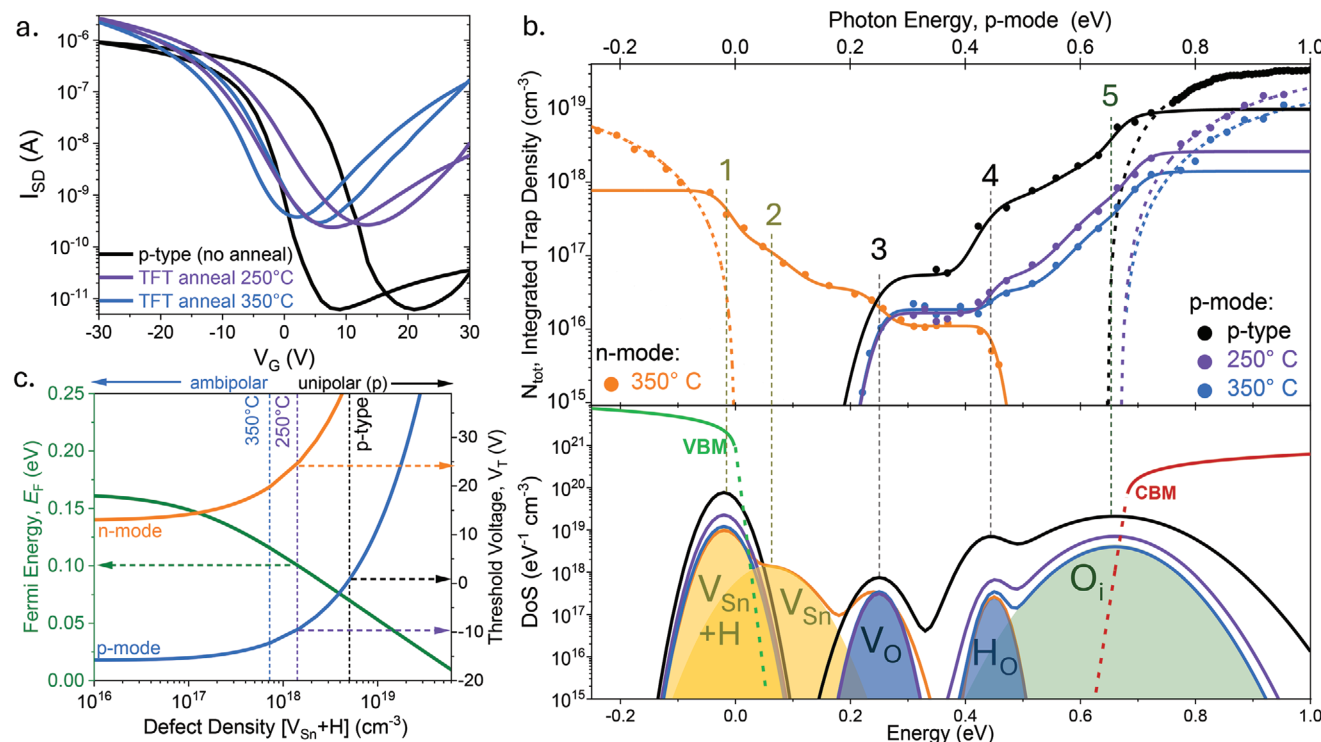

Figure 3. p-type SnO Subgap DoS a) SnO TFT (W/L = 10, V_{SD} = 1 V) transfer curves show unipolar p-type TFT behavior with no post-deposition anneal (black), and increasing ambipolar TFT behavior after annealing at 250 °C (purple) and 350 °C (blue). b) Experimental integrated trap density N_{tot} (upper panel) and subgap DoS (*lower panel*). c) As the concentration of peak 1, $[V_{Sn}$+H], increases, the simulated equilibrium Fermi level energy, E_F (green), moves toward the valence band and the threshold voltage (blue and orange) shifts positively for both p-mode and n-mode behavior, respectively.

© 2025 The Author(s). Advanced Electronic Materials published by Wiley-VCH GmbH

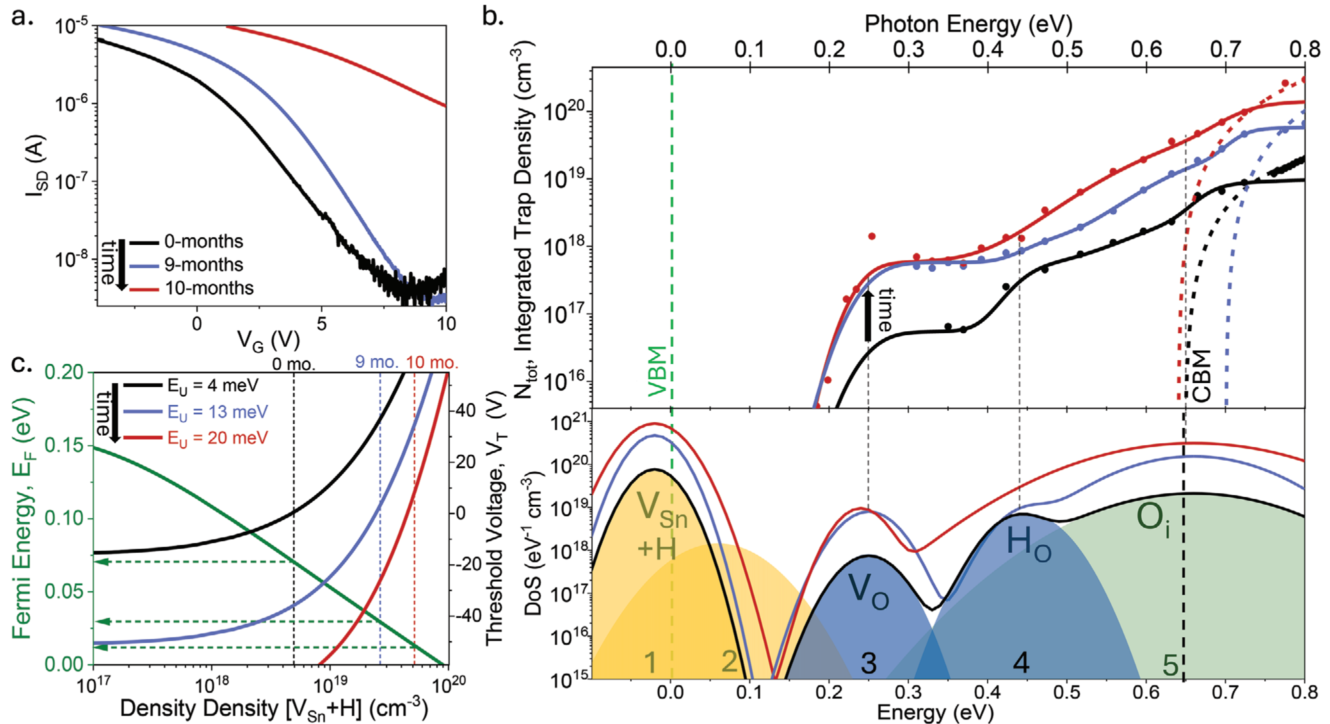

Figure 4. SnO Subgap Trap Density Oxidation. a) SnO TFT (V_{SD} = 1 V, W/L = 100) transfer curve shift with time, from 0-months (black), 9-months (green) to 10-months (cyan) in vacuum storage b) The integrated trap density N_{tot} (upper panel) measured by UP-DoS and corresponding subgap DoS (lower panel) at three vacuum storage times. c) Simulated Fermi level energy, E_F, and threshold voltage, V_T, reveals that the valence band Urbach energy, E_U, increases with time.

2.3. SnO TFT DoS Stability Study

SnO TFT properties change after 0-, 9-, and 10-months of vacuum storage, with a 1-week exposure to lab atmosphere introduced between months 9 and 10. As indicated in **Figure 4a**, the threshold voltage exhibits a large positive shift from 1 V (black), to 3 V (blue), and finally to 8 V (red). Furthermore, the off current further increased dramatically from ≈0.01 µA at 9-months to ≈1 µA at 10-months. Similarly, with increasing time Figure 4b shows a substantial increase in the measured N_{tot} (upper panel) with a corresponding increase of subgap DoS (lower panel). After 10 months, the resulting large increase in the subgap DoS near Peaks 1 suggests the TFT has become so strongly p-type doped that turn-off is unfeasible, as seen in the associated transfer red curve shown in Figure 4a.

Figure 4c plots the simulated Fermi level energy and p-mode threshold voltage as a function of increasing density of tin-vacancy related states, [V_{Sn}+H]. Previously, in the Figure 3c simulation, the valence band Urbach energy extracted was constant at E_U ≈4 meV accurately simulating the three different TFT processing conditions. However, the extracted Urbach energy increases in Figure 4c with the subgap density from E_U ≈ 4 meV at 0 months to E_U ≈13 meV at 9 months, and finally to E_U ≈20 meV after 10 months of vacuum storage.

Since the valence band Urbach energy is a measure of disorder on the anion sublattice, it is reasonable that there may be some correlation between certain subgap peaks and valence band tail states. The observed increase in [V_{Sn}+H] with increasing vacuum storage time is likely associated with the oxidative process, SnO → SnO_2 since this process is known to be associated with tin vacancy formation.[49,50] However, it is also possible that hydrogen incorporation or diffusion could also play a role in SnO TFT degradation.

2.4. Copper Oxide Subgap DoS

The copper oxide TFT transfer curve is unipolar p-type with a 10^4 turn-on, as shown previously in Figure 1b. **Figure 5** presents the associated subgap integrated trap density, N_{tot} in the top panel, and density of states, DoS in the bottom panel. Three N_{tot} clear steps labeled 1–3 are indicated in Figure 5 and correspond to threeGaussian DoS peaks positioned at 0.20, 0.64, and 1.00 eV above the valence band maximum. Proposed defect identifications for these three peaks are labeled in Figure 5 and summarized in **Table 3**.

Proposed peak identifications of the three copper oxide peaks measured are based on DFT calculations by Zivković and de Leeuw, or by Scanlon et al., for CuO or Cu_2O defect site and formation energies.[27,28] The measured 0.20 eV peak is identified as a copper vacancy acceptor, V_{Cu}, comparable to the 0.17 eV value estimate for CuO or the 0.23 eV estimate for Cu_2O. The measured 0.64 eV peak is ascribed to an oxygen-on-copper antisite defect, O_{Cu}, similar to the calculated value of 0.49 eV on the CuO sublattice.[27] Finally, the peak measured at 1.00 eV is ascribed to an oxygen interstitial, O_i, since both phases are calculated to

© 2025 The Author(s). Advanced Electronic Materials published by Wiley-VCH GmbH

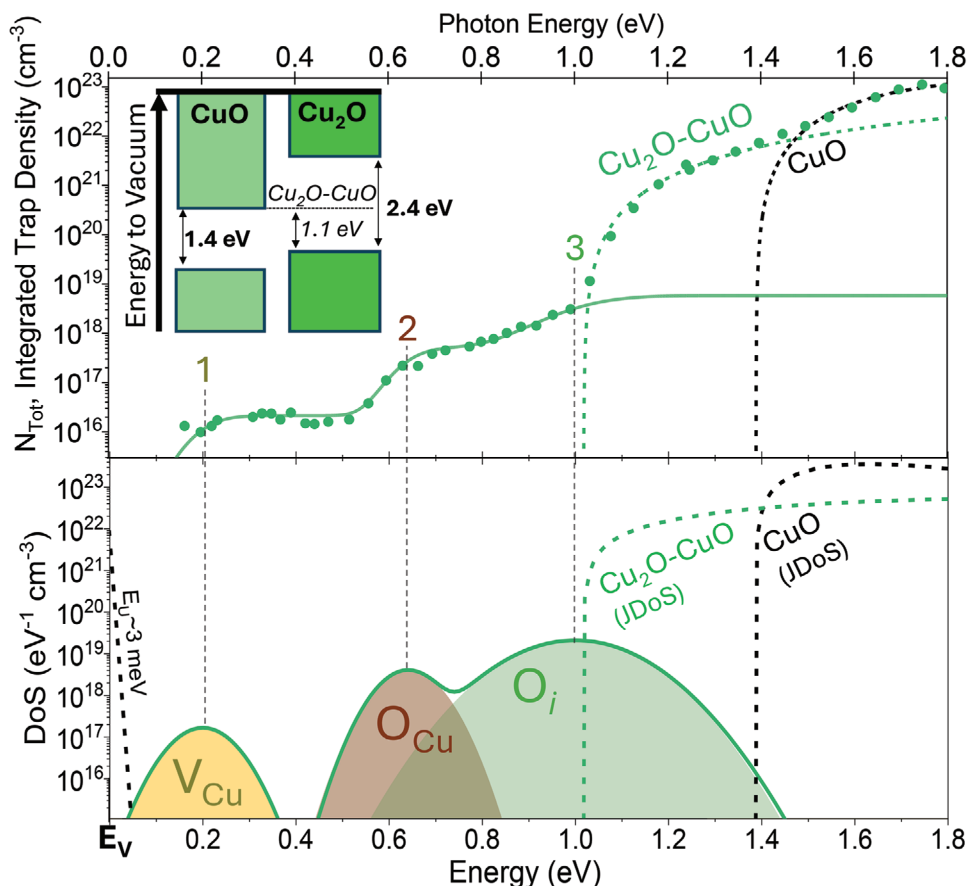

Figure 5. Copper oxide TFT integrated trap density, N_{tot}, (upper panel) and density of states, DoS, (lower panel). The above-bandgap UP-DoS response is fit to indirect transition lineshapes (dashed), while the below-bandgap response displays three clear steps that are fit to error functions. The DoS plot reveals three subgap peaks with suggested defect identifications, as summarized in Table 3. (inset) Band alignment diagram for the mixed-phase system.

have O_i point defects in this portion of the bandgap with predicted ionization energies of 1.14 eV and 1.08 eV for CuO and Cu_2O, respectively.[27,28] Note that the O_i defect in copper oxide, as shown in Figure 5, has a similar relative Gaussian width and position within the subgap as the O_i defect in tin oxide, as shown in Figure 2.

Similar to tin oxide, the measured copper oxide subgap DoS is used to estimate the Fermi level energy and valence band Urbach energy to be $E_F = 260$ meV and $E_U = 3$ meV, respectively. Then, from charge balance, the copper oxide equilibrium hole concentration is estimated to be $p = 2 \times 10^{16}\text{cm}^{-3}$, which is approximately equal to the copper vacancy concentration $p \approx [V_{Cu}]$.

Recall from Figure 1c that the indirect bandgap of copper oxide was estimated to be 1.4 eV, equal to that of CuO based on a linear-regression fit to a Tauc-like plot of normalized photoconductance. However, note that this indirect bandgap estimate is based on ignoring a weaker subgap absorption response with a lower-energy threshold of ≈ 1.1 eV (see Figure 1c). If this weaker subgap absorption response is taken into account, as indicated in Figure 5, it can only be included as an above-bandgap feature (in which the DoS is given by a quadratic function of energy), rather than a below-bandgap feature (in which the DoS is described by a Gaussian function of energy). This suggests that the indirect bandgap of copper

Table 3. Estimated subgap DoS peak parameters from UP-DoS measurements of the copper oxide TFT plotted in Figure 5. Experimental results are compared to DFT calculated values by Zivković and de Leeuw. [27] The UP-DoS results and DFT show excellent agreement both in terms of relative defect prevalence and defect peak energy.

DoS Peak	Assigned Defect	Peak Energy [eV]	FWHM [meV]	Peak DoS × 10^{17} [$\text{cm}^{-3}\text{eV}^{-1}$]	DFT Formation Energy[27] [eV]	DFT Peak Energy[27] [eV]
1	V_{Cu}	0.20	50	1.6	1.0	0.17
2	O_{Cu}	0.64	48	40	0.5	0.49
3	O_i	1.00	99	210	0.3	1.14

 © 2025 The Author(s). Advanced Electronic Materials published by Wiley-VCH GmbH

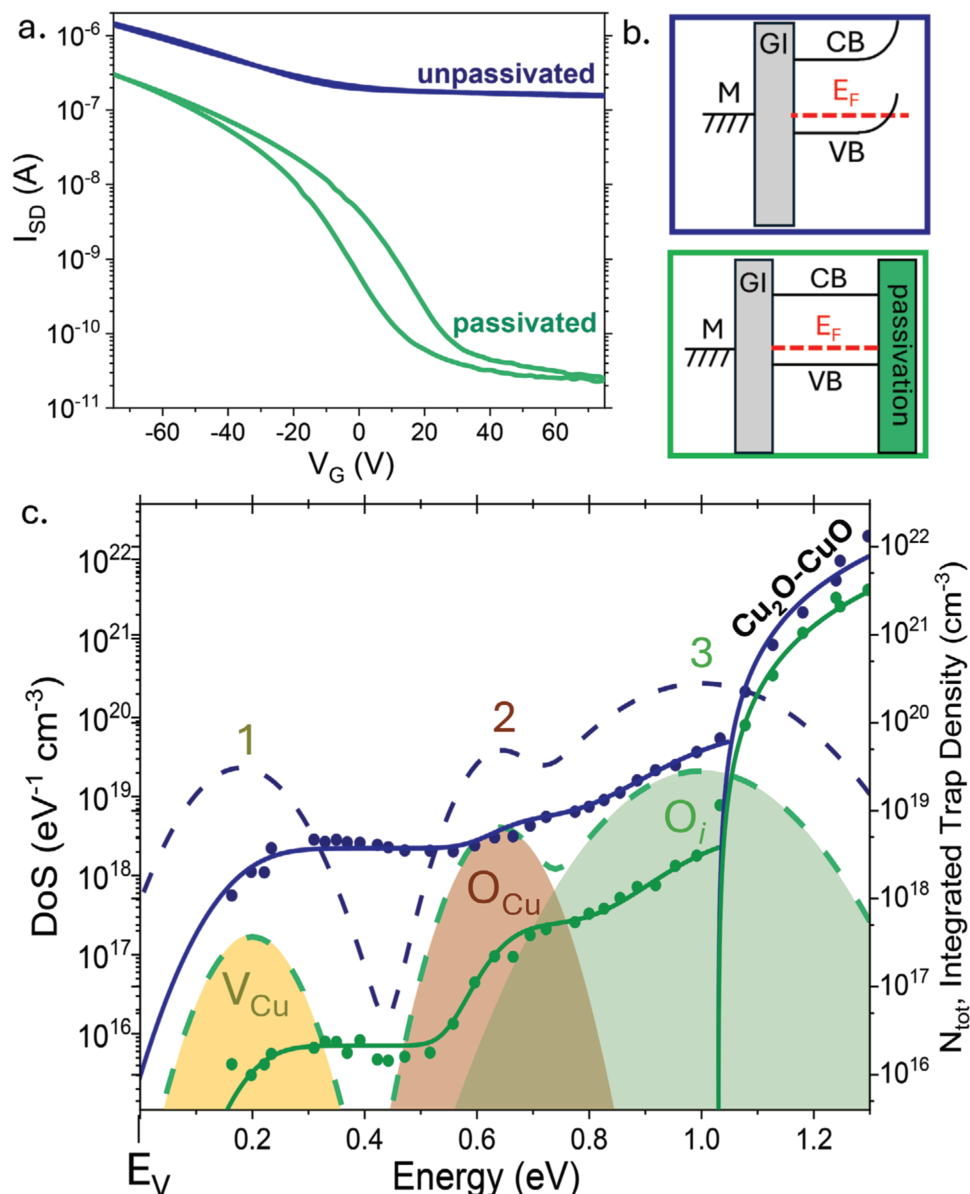

Figure 6. a) Transfer curves of unpassivated and passivated copper oxide TFTs at V_{SD} = 1 V (W/L = 10). b) Band diagrams illustrate the strong back-channel band bending expected in the unpassivated device at equilibrium. c) DoS (dashed lines, left axis) and integrated trap density (solid lines, right axis) of the unpassivated and passivated copper oxide TFT.

oxide is actually equal to 1.1 eV rather than 1.4 eV, as expected for CuO.

How do we rationalize the physics of this 1.1 eV lower-energy threshold since it appears to be inconsistent with both CuO and Cu_2O? We propose that this 1.1 eV lower-energy threshold is a mixed-phase transition involving real-space electron transfer in which a filled initial electronic state at the Cu_2O valence band maximum is excited into an empty final electronic state at the CuO conduction band minimum. Such a process is accomplished by real-space electron transfer from the Cu_2O (filled) initial state into the CuO (empty) final state and is labeled in Figure 5 as a Cu_2O-CuO (mixed phase) transition. Khoo et al. estimate the energy difference from the Cu_2O valence band to the CuO conduction band to be 1.09 eV, in good agreement with our observed 1.1 eV threshold energy.[36] Figure 5 *inset* shows the estimated energy band alignment for the mixed-phase copper oxide.

2.5. Unpassivated and Passivated Copper Oxide Subgap DoS

While all TFTs previously discussed have been passivated with a 20 nm layer of aluminum oxide, **Figure 6a** compares the transfer curves of copper oxide TFTs when the back-channel is passivated (green) or unpassivated (blue). The unpassivated device has a high-off current and no clear turn-off voltage. Figure 6b illustrates energy band diagrams showing the existence of a backside

© 2025 The Author(s). Advanced Electronic Materials published by Wiley-VCH GmbH

accumulation layer responsible for the poor performance exhibited by the unpassivated TFT. In contrast, passivation eliminates the back-side accumulation layer and its deleterious effect on TFT performance. Figure 6c presents a comparison of N_{tot} and DoS for an unpassivated and passivated copper oxide TFT. Consistent with prior studies, the degraded performance of the unpassivated TFT appears to correlate with the enhanced defect DoS across the entire subgap.[51] This result suggests that an increase in charged copper vacancies at the backside may be responsible for the formation of this additional accumulation layer.

2.6. Defect Peak Validation using Recombination Lifetimes in P-Type TFTs

In tin and copper oxide TFTs, Tables 1–3 summarize how literature DFT that predict relative defect abundance and energies, closely match the UP-DoS measured bandgaps, defect peak energies, and relative peak amplitude trends. For experimental validation of UP-DoS peak identity, prior studies on a-IGZO TFTs assign DoS peaks using TFT photoconduction fall times that change abruptly for oxygen versus metal vacancy subgap excitations.[5] Similarly, in both copper oxide (left panel) and ambipolar tin oxide (right panel) TFTs, **Figure 7a** shows the exponentially-fitted p-mode photoconduction fall time (τ_p) decreases with increasing incident photon energy. In copper oxide, Figure 7b shows the extracted τ_p (open circles) times are anti-correlated with overlaid integrated trap density N_{tot} (green circles, right axis). Specifically, the fall times decrease abruptly with each successive V_{Cu}, O_{Cu}, and O_i subgap Gaussian defect peaks labeled. Collectively, with increasing photon energy, the fall times show a stepwise decrease as each new defect peak becomes optically accessible.

Figure 7c plots TFT fall times in SnO ambipolar TFTs that also decrease with increasing incident photon energy for p-mode TFT operation. Overlaid is the measured respective dominant subgap states photo-excited for p-mode (*blue*) and n-mode (*orange*) operation. The fall times are observed to evolve successively for each peak in the overlaid DoS, independently matching the UP-DoS subgap peak progression. Importantly, near $h\nu \approx 0.7$ eV, both n- and p-mode fall times merge to match at $\tau_{p/n} \approx 280$ µs, suggesting both photoexcitations are dominated by relaxation from the same band-edge defect site ascribed to the V_{Sn}+H acceptor DoS band-edge peak.

To further explore the midgap region of SnO, tunable laser excitations down to 0.5 eV show extracted fall time τ_p increases tenfold to ≈2.5 ms for p-mode gate voltages. Prior UP-DoS fall time studies demonstrate that charge-neutral defect states have inherently longer fall times than ionized defects due to the weaker Coulombic interaction mediating recombination.[5] Such p-mode mid-gap photoexcitations in SnO suggest that empty deep donors photoexcitation proceeds as $V_O^+ + h\nu \rightarrow V_O{}^0 + h^+$ to create a neutral filled donor. Consequently, the rapidly changing TFT fall times in SnO independently support the Table 2 identification of peaks 3–4 as donors and peaks 1 and 5 as acceptor states. By contrast, for copper oxide, the 7b fall times only increase by ≈2 ×, implying all subgap defects are of a similar nature, in agreement with Table 3, which suggests all subgap peaks aare all acceptor-like.

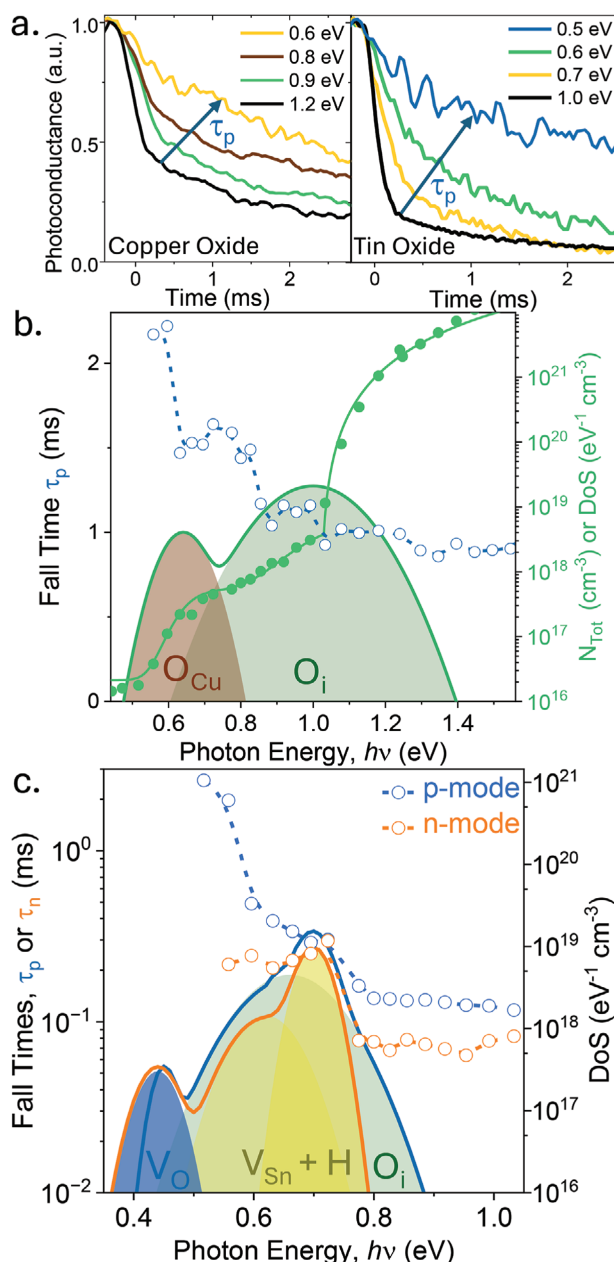

Figure 7. a) Copper (left) and tin (right) oxide transient photoconduction curves. b) Copper oxide TFT fall times (blue) decrease as the subgap trap density, N_{tot} (right axis) increases with photon energy. c) Tin oxide TFT photoconduction fall times for n-mode operation (orange) and p-mode operation (blue) change abruptly as each successive overlaid DoS peak becomes optically accessible.

With the aid of recombination lifetimes, the UP-DoS method provides the full TFT subgap DoS with peak identity characterization. In contrast, established methods on the tin and copper oxide primarily characterize band-edges by CV,[29] and elemental analysis by x-ray photoelectron spectroscopy (XPS),[36,47] and electron energy loss spectroscopy[21,52,53] (see Section S5, Supporting Information). Recently, a XPS study shows tin oxide has a surplus of elemental oxygen that they similarly ascribed to prevalent

© 2025 The Author(s). Advanced Electronic Materials published by Wiley-VCH GmbH

oxygen interstitial defects.[47] Such emerging independent studies strongly agree with our tin oxide UP-DoS analysis that further shows this oxygen interstitial defect density critically determines when TFTs transition from ambipolar to the desirable unipolar p-type metal oxide TFT behavior.

3. Conclusion

Tin oxide and copper oxide constitute two possible material strategies for realizing p-type oxide TFTs. For each TFT, the subgap integrated trap density is measured over a tunable $h\nu = 0.15 - 3.5$ eV laser excitation range using the ultrabroadband photoconduction DoS (UP-DoS) technique.[5,6,54] The below-gap photoconductivity drops off by $\approx 10^5$ in tin oxide and $\approx 10^7$ in copper oxide and indicates how the corresponding SnO and CuO material phases drive p-type conductivity in each TFT.

Measuring subgap integrated traps in n-mode and p-mode for ambipolar TFTs provides two complimentary DoS spectra that fully span the subgap. In tin oxide, the resulting subgap DoS shows five subgap peaks assigned as: tin vacancies (V_{Sn} and V_{Sn}+ H), oxygen vacancies in the midgap (V_O and H_O), and oxygen interstitial sites. The broad oxygen interstitial peak adjacent to the CB-edge suppresses n-mode conduction to achieve the desired unipolar p-mode TFT behavior with low off current. The near VB-edge tin vacancy V_{Sn}+ H peak determines the TFT equilibrium Fermi level energy and p-doping, such that $p \approx [V_{Sn} + \mathrm{H}]$. By using the measured subgap DoS together with detailed charge balance and the discrete trap model, a framework is created where the defect concentration, $[V_{Sn}+\mathrm{H}]$, and the Fermi level energy is accurately estimated solely from the threshold voltage of the device.

For p-type copper oxide TFTs, the subgap DoS shows just three subgap peaks assigned as: copper vacancies near the VB-edge, oxygen-on-copper antisites in the mid-gap, and oxygen interstitial sites near the CB-edge. Similar to the tin oxide case, the metal vacancy peak, V_{Cu}, determines the TFT p-doping, such that $p \approx [V_{Cu}]$. The copper oxide thin-film growth that was employed tends to favor the formation of Cu_2O, a wider bandgap p-type semiconductor with some inadvertent incorporation of CuO, a narrow bandgap p-type semiconductor with a poor mobility. Even though the oxidized CuO is likely only prevalent near the semiconductor-dielectric interface, its lower bandgap is likely responsible for the low field-effect mobility in the copper oxide TFTs. Careful consideration of the observed CuO-Cu_2O heterojunction interface may also be central to improving p-type TFT performance. Nonetheless, synthesis of a phase-pure Cu_2O thin-film appears to be a challenging but desirable goal.

4. Experimental Section

Preparation of P-Type TFTs: Each TFT fabrication approach was based upon methodologies developed for tin oxide and copper oxide TFTs.[39,40] Bottom gate, top contact TFTs were fabricated with a thermally-grown SiO_2 (thickness, $t = 200$ nm) as the gate dielectric and heavily-doped p-type Si (100) substrate as the gate electrode. Thermally evaporated gold ($t = 100$ nm) was used as the source and drain contacts. The channel layer and the contacts were patterned by photolithography with either lift-off or wet etching method. Unless otherwise stated, the back channel was passivated with Al_2O_3 ($t = 20$ nm) by atomic layer deposition (ALD) in all devices. For a width-to-length ratio (W/L) of 10, the TFTs reported have a channel width and length of 1000 µm and 100 µm.

The SnO channel layer was deposited by ALD using Sn(II) bis-(tert-butoxide) and water at a substrate temperature of 170 °C. By varying SnO thickness and process conditions, TFTs exhibit either depletion mode (for TFTs, D1 and D2) or enhancement modes (E1 and E2), as shown in Table S2 (Supporting Information). TFTs incorporating a thicker SnO layer are expected to have a high carrier concentration (D1 and D2), therefore the device operates in depletion mode and the current conduction (mobility) depends on the annealing temperatures. On the other hand, devices E1 and E2 incorporate a more resistive and thinner SnO layer, thus requiring two annealing steps. Even though the μ_{FE} was similar, E2 with a higher TFT annealing temperature exhibits ambipolar properties, while E1 with a lower TFT annealing temperature exhibits predominantly p-type characteristics.

The Cu_2O channel layer ($t = 260$ nm) was deposited in a high target utilization sputtering system from a metallic target. A post-deposition annealing was performed at 700 °C after the channel patterning. The unpassivated Cu_2O TFT exhibits a field effect mobility, μ_{FE} of 0.21 $cm^2V^{-1}s^{-1}$ with a small on-off ratio ≈ 10. In the passivated device, the on-off ratio increases significantly to $\approx 10^4$ but with a reduced on-state current, thus μ_{FE} of 0.07 $cm^2V^{-1}s^{-1}$. To prevent device breakdown, the SnO TFTs were limited to gate voltages within the range of $V_g = \pm 30$ V owing to the small bandgap, whereas Cu_2O, can typically be safely scanned up to $V_g = \pm 75$ V.

Post-growth analysis suggests that Cu_2O and SnO should be the dominant materials present in each TFT.[39,40] However, the active channel was known to readily oxidize to CuO and SnO_2.[55,56] Before measurements, the absorption spectra (Cary UV–Vis–IR) for tin and copper oxide thin-films derived from the TFT growths were compared to the corresponding TFT photoconduction(PC) spectra.

TFT Ultrabroadband Photoconductance Density of States (UP-DoS) Microscopy: The Ultrabroadband Photoconduction Density of States (or UP-DoS) microscopy method was applied to tin and copper oxide TFTs to measure the subgap defect density.[5,6,54,57] Figure 1a depicts the UP-DoS setup measuring the photoconduction, $I_{PC}(h\nu)$ on a TFT with an ultrabroadband tunable laser from photon energies of $h\nu = 0.15$ to 3.5 eV. To achieve photon energies for near mobility edge excitation, a home-built difference-frequency generation mixes OPO signal and idler beam overlap on an HGS crystal that produces a tunable laser up to 10,000nm. [58] The diffraction-limited laser illuminates a tin or copper oxide active channel from the top side through the thin passivation layer of aluminum oxide. The TFT gate voltage was carefully selected to ensure that the TFT transfer curve is a quasi-linear regime, such that the small incident photon flux ($\approx 10^{13}$ photons/cm^2) induces a small linear shift in the illuminated transfer curve.[5] The TFT conductivity was continuously monitored with a custom-built RF probe microscopy station that uses all-reflective 4*f*-scanning optics. A high-NA (0.65) 52x reflective objective delivers a nearly diffraction-limited tunable-laser. The bottom panel of Figure 1a shows this 1.1 eV laser mapping the TFT I_{PC} response over the copper oxide TFT active region.

To measure the DoS of a TFT, the primary observable was the photon-normalized photoconduction, $I_{\mathrm{norm}}(h\nu) = h\nu I_{PC}/P$, where I_{PC} is the Zurich lock-in amplifier (HFLI) detected photoconduction signal., and P is the incident laser power (ranges from ≈ 0.1 to 100 µW). I_{norm} has units of $\mathrm{AeV^{-1}W^{-1}}$. Providing $h\nu < E_g$, only band-to-defect (p-mode) or defect-to-band (n-mode) transitions are likely, and the detected signal I_{norm} can be approximated as,

$$I_{\mathrm{norm}}^{\mathrm{p-mode}}(h\nu) \propto N_{filled}^{VB} \int_{-\infty}^{\infty} N_{empty}(E + h\nu)dE \quad (1)$$

$$I_{\mathrm{norm}}^{\mathrm{n-mode}}(h\nu) \propto N_{empty}^{CB} \int_{-\infty}^{\infty} N_{filled}(h\nu - E)dE \quad (2)$$

where $N_{empty}(E + h\nu)$ is the subgap DoS of empty defect states excited to with photon energy $h\nu$ from filled valence band states, N_{filled}^{VB}, in p-mode

© 2025 The Author(s). Advanced Electronic Materials published by Wiley-VCH GmbH

operation. $N_{filled}(h\nu - E)$ was the subgap DoS of filled defect states that were excited to empty conduction band states, N^{CB}_{empty}, in n-mode operation. See Section S1 (Supporting Information) for a comparison when $h\nu > E_g$.

To obtain the absolute integrated total defect density per unit volume, N_{tot}, the directly measured quantity $I_{\rm norm}(h\nu)$ is simply rescaled by a constant given in the bracketed expression below,[5]

$$N_{tot}(h\nu) = I_{\rm norm}(h\nu)\left[\frac{C_{ox}k_o}{qd}\left(\frac{\partial I_D}{\partial V_G}\right)^{-1}\right] \quad (3)$$

where C_{ox} is the gate oxide capacitance of the TFT, q is the charge of the electron, d is the thickness of the excited accumulation channel (≈0.3 nm). $(\frac{\partial I_D}{\partial V_G})$ is the non-illuminated slope of the TFT transfer curve in the linear regime where the UP-DoS measurement was conducted. k_o is the rate of incident photons that causes the I_{PC} signal to saturate owing to state filling (or $k_o \approx \frac{P_{sat}}{h\nu}$). Finally, the first derivative of Equation (3) with respect to energy provides the desired experimental subgap DoS as $\frac{dN_{Tot}}{d(h\nu)}$. To further validate the results of UP-DoS, a complementary measurement of TFT photoconduction fall times was conducted. The TFT photoconduction fall time traces are captured by a Tektronix TDS 3054B 500 MHz oscilloscope triggered to the mechanical chopping of the tunable laser sources at 200 Hz.

The UP-DoS method signal measured derived from the free carrier density excited by optically-allowed defect-to-band (n-mode), and band-to-defect (p-mode) transitions. The TFT further requires broadband access to the tunable femtosecond lasers that could measure the mobility band-edge states to within 0.12 eV of the bandgap. A complete discussion of limitations associated with the UP-DoS method is provided in Section S4 (Supporting Information).

TFT Simulation by Charge Balance and Discrete Trap Model: By using the experimental full subgap functional form of all measured subgap DoS peaks shown in Figures 3b and 4b, a discrete trap model together with charge balance simulates the equilibrium Fermi energy, TFT threshold voltages, and Urbach tail energies. The equation for charge balance involved a balance between positive and negative charges,

$$N^+_{GD}(E_F) + N^+_{TD}(E_F) + p(E_F) = N^-_{GA}(E_F) + n(E_F) \quad (4)$$

where (N^+_{GD}) is ionized Gaussian donors, (N^+_{TD}) is ionized valence band tail donors, (N^-_{GA}) is filled Gaussian acceptors, and n/p is free electron/hole density (see Section S2, Supporting Information for the full functional form evaluated using a Fermi-Dirac statistics at 295 K). The corresponding equation for the discrete acceptor trap model is:[59]

$$V_T(E_F) = -\frac{q}{C_I}\left[{N^0_{TD}}^{\frac{2}{3}} + {N^0_{GD}}^{\frac{2}{3}} + {N^-_{GA}}^{\frac{2}{3}} - p^{\frac{2}{3}}\right] \quad (5)$$

where q is electron charge, and C_I is the gate insulator capacitance density. The final results for V_T and E_F are plotted in Figures 3c and 4c. Note that the only two parameters not measured by UP-DoS in Equations (4) and Equation (5) were the fermi level energy, E_F, and the valence band tail donors (N^+_{TD} or N^0_{TD}), whereas (N^+_{TD} or N^0_{TD}) further only depends on E_F, the hole effective mass m^*_h, and valence band Urbach energy E_U.[19] By using literature-reported values of m^*_h,[60–62] the system of equations could be solved for the two unknowns, E_F and E_U. Similarly, by instead using the discrete trap donor model,[59] the conduction band Urbach energy could be estimated. Finally, once E_U is known, using the equations above, the Fermi level energy is simulated together with n- and p-mode threshold voltages, and plotted versus band edge defect concentration.

Supporting Information

Supporting Information is available from the Wiley Online Library or from the author.

Acknowledgements

This work was supported by a SAMSUNG Global Research Outreach (GRO) Award. KMN and AJF acknowledged support from EPSRC EP/X025195/1, 'Innovative Material, Processes, and Devices for Low Power Flexible Electronics: Creating a Sustainable Internet of Everything.'

Conflict of Interest

The authors declare no conflict of interest.

Data Availability Statement

The data that support the findings of this study are available from the corresponding author upon reasonable request.

Keywords

CMOS, copper oxide, defect characterization, thin-film transistors, tin oxide

Received: December 11, 2024
Revised: January 26, 2025
Published online:

[1] A. Nathan, S. Lee, S. Jeon, J. Robertson, *J. Disp. Technol.* **2014**, *10*, 917.
[2] G. Wakimura, Y. Yamauchi, Y. Kamakura, *J. Adv. Simul. Sci. Eng.* **2015**, *2*, 201.
[3] J. F. Wager, B. Yeh, R. L. Hoffman, D. A. Keszler, *Curr. Opin. Solid State Mater. Sci.* **2014**, *18*, 53.
[4] H. Hosono, *Nat. Electron.* **2018**, *1*, 428.
[5] K. T. Vogt, C. E. Malmberg, J. C. Buchanan, G. W. Mattson, G. M. Brandt, D. B. Fast, P. H.-Y. Cheong, J. F. Wager, M. W. Graham, *Phys. Rev. Res.* **2020**, *2*, 033358.
[6] G. W. Mattson, K. T. Vogt, J. F. Wager, M. W. Graham, *Adv. Funct. Mater.* **2023**, *33*, 2300742.
[7] Z. Wang, P. K. Nayak, J. A. Caraveo-Frescas, H. N. Alshareef, *Adv. Mater.* **2016**, *28*, 3831.
[8] Z. Ouyang, W. Wang, M. Dai, B. Zhang, J. Gong, M. Li, L. Qin, H. Sun, *Materials* **2022**, *15*, 4781.
[9] N. Devabharathi, S. Yadav, I. Dönges, V. Trouillet, J. J. Schneider, *Adv. Mater. Interfaces* **2024**, *11*, 2301082.
[10] W. Xu, J. Zhang, Y. Li, L. Zhang, L. Chen, D. Zhu, P. Cao, W. Liu, S. Han, X. Liu, et al., *J. Alloys Compd.* **2019**, *806*, 40.
[11] J. H. Lee, J. Kim, M. Jin, H.-J. Na, H. Lee, C. Im, Y. S. Kim, *ACS Appl. Electron. Mater.* **2023**, *5*, 1123.
[12] E. Fortunato, R. Barros, P. Barquinha, V. Figueiredo, S.-H. K. Park, C.-S. Hwang, R. Martins, *Appl. Phys. Lett.* **2010**, *97*, 5.
[13] Y. Ogo, H. Hiramatsu, K. Nomura, H. Yanagi, T. Kamiya, M. Hirano, H. Hosono, *Appl. Phys. Lett.* **2008**, *93*, 3.
[14] L. Lan, J. Peng, *IEEE Trans. Electron Devices* **2011**, *58*, 1452.
[15] K. Nomura, H. Ohta, A. Takagi, T. Kamiya, M. Hirano, H. Hosono, *Nature* **2004**, *432*, 488.
[16] Y. Jang, J. Park, J. Kang, S.-Y. Lee, *ACS Appl. Electron. Mater.* **2022**, *4*, 1427.
[17] A. Belmonte, H. Oh, S. Subhechha, N. Rassoul, H. Hody, H. Dekkers, R. Delhougne, L. Ricotti, K. Banerjee, A. Chasin, et al., in *2021 IEEE International Electron Devices Meeting (IEDM)*, IEEE, Piscataway, NJ **2021**, pp. 10.6.1–10.6.4.

 © 2025 The Author(s). Advanced Electronic Materials published by Wiley-VCH GmbH

[18] K. Iordanidou, C. Persson, *Mater. Sci. Semicond. Process.* **2021**, *121*, 105297.
[19] J. F. Wager, *AIP Adv.* **2017**, *7*, 12.
[20] Y. Hu, D. Schlom, S. Datta, K. Cho, *ACS Appl. Mater. Interfaces* **2022**, *14*, 25670.
[21] Y. Wang, S. Lany, J. Ghanbaja, Y. Fagot-Revurat, Y. P. Chen, F. Soldera, D. Horwat, F. Mücklich, J. Pierson, *Phys. Rev. B* **2016**, *94*, 245418.
[22] E. Fortunato, V. Figueiredo, P. Barquinha, E. Elamurugu, R. Barros, G. Gonçalves, S.-H. K. Park, C.-S. Hwang, R. Martins, *Appl. Phys. Lett.* **2010**, *96*, 19.
[23] A. Sekkat, V. H. Nguyen, C. A. Masse de La Huerta, L. Rapenne, D. Bellet, A. Kaminski-Cachopo, G. Chichignoud, D. Mu noz-Rojas, *Commun. Mater.* **2021**, *2*, 78.
[24] A. Togo, F. Oba, I. Tanaka, K. Tatsumi, *Phys. Rev. B* **2006**, *74*, 195128.
[25] A. W. Lee, D. Le, K. Matsuzaki, K. Nomura, *ACS Appl. Electron. Mater.* **2020**, *2*, 1162.
[26] J. P. Allen, D. O. Scanlon, L. F. Piper, G. W. Watson, *J. Mater. Chem. C* **2013**, *1*, 8194.
[27] A. Zivković, N. H. de Leeuw, *Phys. Rev. Mater.* **2020**, *4*, 074606.
[28] D. O. Scanlon, B. J. Morgan, G. W. Watson, A. Walsh, *Phys. Rev. Lett.* **2009**, *103*, 096405.
[29] A. W. Lee, Y. Zhang, C.-H. Huang, K. Matsuzaki, K. Nomura, *Adv. Electron. Mater.* **2020**, *6*, 2000742.
[30] C.-Y. Jeong, D. Lee, Y.-J. Han, Y.-J. Choi, H.-I. Kwon, *Semicond. Sci. Technol.* **2015**, *30*, 085004.
[31] H. Luo, L. Liang, H. Cao, M. Dai, Y. Lu, M. Wang, *ACS Appl. Mater. Interfaces* **2015**, *7*, 17023.
[32] Y. Wu, Z. Tang, G. J. Cruz, Y. Yang, W. Zhang, W. Ren, P. Zhang, *Phys. Rev. B* **2022**, *106*, 085201.
[33] K. J. Saji, Y. V. Subbaiah, K. Tian, A. Tiwari, *Thin Solid Films* **2016**, *605*, 193.
[34] W. Guo, L. Fu, Y. Zhang, K. Zhang, L. Liang, Z. Liu, H. Cao, X. Pan, *Appl. Phys. Lett.* **2010**, *96*, 4.
[35] W. Zhou, Y. Liu, Y. Yang, P. Wu, *J. Phys. Chem. C* **2014**, *118*, 6448.
[36] P. Khoo, K. Satou, M. Izaki, in *IOP Conference Series: Materials Science and Engineering*, vol. *920*, IOP Publishing, Bristol, England **2020**, p. 012028.
[37] D. Ozaslan, O. Erken, M. Gunes, C. Gumus, *Phys. B* **2020**, *580*, 411922.
[38] J. Varley, A. Schleife, A. Janotti, C. Van de Walle, *Appl. Phys. Lett.* **2013**, *103*, 8.
[39] D. E. Gomersall, K. M. Niang, J. D. Parish, Z. Sun, A. L. Johnson, J. L. MacManus-Driscoll, A. J. Flewitt, *J. Mater. Chem. C* **2023**, *11*, 5740.
[40] S. Han, K. M. Niang, G. Rughoobur, A. J. Flewitt, *Appl. Phys. Lett.* **2016**, *109*, 17.
[41] J. Jo, J. D. Lenef, K. Mashooq, O. Trejo, N. P. Dasgupta, R. L. Peterson, *IEEE Trans. Electron Devices* **2020**, *67*, 5557.
[42] L. Guo, M. Zhao, D.-M. Zhuang, M. Cao, L. Ouyang, X. Li, R. Sun, Z. Gao, *Appl. Surf. Sci.* **2015**, *359*, 36.
[43] V. Singh, J. Sinha, S. Shivashankar, S. Avasthi, *J. Mater. Chem. C* **2023**, *11*, 7356.
[44] S. Im, Y.-G. Chang, J. H. Kim, *Photo-Excited Charge Collection Spectroscopy: Probing the traps in field-effect transistors*, Springer Science & Business Media, Berlin, Heidelberg **2014**.
[45] F.-Y. Ran, M. Taniguti, H. Hosono, T. Kamiya, *J. Disp. Technol.* **2015**, *11*, 720.
[46] F. Oba, M. Choi, A. Togo, A. Seko, I. Tanaka, *J. Phys.: Condens. Matter* **2010**, *22*, 384211.
[47] M. Januar, C.-Y. Lu, H.-C. Lin, T.-Y. Huang, C.-M. Yang, K.-K. Liu, K.-C. Liu, *Mater. Adv.* **2024**, *5*, 4679.
[48] J. F. Wager, *Amorphous Oxide Semiconductors: IGZO and Related Materials for Display and Memory*, Wiley, New York **2022**, pp. 105–123.
[49] T. Leijtens, R. Prasanna, A. Gold-Parker, M. F. Toney, M. D. McGehee, *ACS Energy Lett.* **2017**, *2*, 2159.
[50] F. Hao, C. C. Stoumpos, D. H. Cao, R. P. Chang, M. G. Kanatzidis, *Nat. Photonics* **2014**, *8*, 489.
[51] M. Napari, T. N. Huq, D. J. Meeth, M. J. Heikkilä, K. M. Niang, H. Wang, T. Iivonen, H. Wang, M. Leskela, M. Ritala, et al., *ACS Appl. Mater. Interfaces* **2021**, *13*, 4156.
[52] M. Moreno, R. Egerton, P. Midgley, *Phys. Rev. B– Condens. Matter Mater. Phys.* **2004**, *69*, 233304.
[53] M. Moreno, R. Egerton, J. Rehr, P. Midgley, *Phys. Rev. B– Condens. Matter Mater. Phys.* **2005**, *71*, 035103.
[54] G. W. Mattson, K. T. Vogt, J. F. Wager, M. W. Graham, *J. Appl. Phys.* **2022**, *131*, 105701.
[55] Y. Alajlani, F. Placido, A. Barlow, H. O. Chu, S. Song, S. U. Rahman, R. De Bold, D. Gibson, *Vacuum* **2017**, *144*, 217.
[56] C. K. G. Kwok, Y. Wang, X. Shu, K. M. Yu, *Appl. Surf. Sci.* **2023**, *627*, 157295.
[57] K. T. Vogt, M. J. Mattsson, M. W. Graham, *U.S. Patent No. 18/885,410*, **2024**, United States Patent and Trademark Office, pending.
[58] M. Beutler, I. Rimke, E. Büttner, V. Badikov, V. Petrov, *JOSA B* **2016**, *33*, D7.
[59] D. Hong, G. Yerubandi, H. Chiang, M. Spiegelberg, J. Wager, *Crit. Rev. Solid State Mater. Sci.* **2008**, *33*, 101.
[60] Y. Ogo, H. Hiramatsu, K. Nomura, H. Yanagi, T. Kamiya, M. Kimura, M. Hirano, H. Hosono, *Phys. Status Solidi A* **2009**, *206*, 2187.
[61] F. Koffyberg, F. Benko, *J. Appl. Phys.* **1982**, *53*, 1173.
[62] J. Hodby, T. Jenkins, C. Schwab, H. Tamura, D. Trivich, *J. Phys. C: Solid State Phys.* **1976**, *9*, 1429.

© 2025 The Author(s). Advanced Electronic Materials published by Wiley-VCH GmbH